Constraints on the composition and temperature of LLSVPs from seismic properties of lower mantle minerals

Kenny Vilella[a,b,*], Thomas Bodin[c], Charles-Edouard Boukaré[d], Frédéric Deschamps[b], James Badro[e], Maxim D. Ballmer[g,f], Yang Li[h]

[a]*JSPS International Research Fellow, Hokkaido University, Japan*
[b]*Institute of Earth Sciences, Academia Sinica, Taipei, Taiwan*
[c]*Univ Lyon, Univ Lyon 1, ENSL, CNRS, LGL-TPE, F-69622, Villeurbanne, France*
[d]*Earth and Planetary Science Laboratory, École Polytechnique Fédérale de Lausanne, Lausanne, Switzerland*
[e]*Institut de Physique du Globe, Univ. Paris Diderot, Sorbonne Paris Cité, CNRS, Paris, France*
[f]*Institute of Geophysics, Department of Earth Sciences, ETH Zurich, Zurich, Switzerland*
[g]*University College London, Department of Earth Sciences, London, UK*
[h]*State Key Laboratory of Lithospheric Evolution, Institute of Geology and Geophysics, Chinese Academy of Sciences*

Abstract

Seismic observations have suggested the presence of two Large Low Shear Velocity Provinces (LLSVPs) in the lowermost mantle whose nature and origin are still debated. Several studies have tried to infer their potential composition using seismic observations with the hope to identify their formation mechanism. In particular, compositions enriched in iron ($\sim 12 - 14$ wt%) and bridgmanite (~ 90 vol%) have been identified as promising candidates. Interestingly, these characteristics are somewhat consistent with the cumulates produced by the solidification of a primitive magma ocean, except that the iron enrichment should be much larger (> 20 wt%). Here, we provide a reappraisal of potential LLSVPs compositions based on an improved mineralogical model including, in particular, the effects of alumina. We systematically investigate the effects of six parameters: FeO and Al_2O_3 content, proportion of $CaSiO_3$ and bridgmanite (so that the proportion of ferropericlase is implicitly investigated), $Fe^{3+}/\sum Fe$ and temperature contrast between far-field mantle and LLSVPs. From the 81 millions

---

*Corresponding author
Email address:* `kennyvilella@gmail.com` (Kenny Vilella)

cases studied, only 79000 cases explain the seismic observations. Nevertheless, these successful cases involve a large range of parameters with, for instance, FeO content between 12–25 wt% and Al_2O_3 content between 3–17 wt%. We then apply a principal component analysis (PCA) to these cases and find two robust results: (i) the proportion of ferropericlase should be low (<6vol%); (ii) the formation of Fe^{3+}-bearing bridgmanite is much more favored compared to other iron-bearing components. Following these results, we identify two end-member compositions: a Bm-rich and a CaPv-rich one. For each end-member composition, a large range of parameters is possible. We note, however, that a low temperature contrast (<500 K) is favored, and that a certain proportion between FeO content, Al_2O_3 and oxidation state should be maintained. Finally, we discuss different scenarios for the formation of LLSVPs and propose that investigating the mineral proportion produced by each scenario is the best way to evaluate their relevance. For instance, the solidification of a primitive magma ocean may produce FeO and Al_2O_3 contents similar to those suggested by our analysis. However, the mineral proportion of such reservoirs is not well-constrained and may contain a larger proportion of ferropericlase than what is allowed by our results.

1. Introduction

The emergence of tomographic models has led to an increased knowledge of the structure and composition of the Earth's mantle. A key result provided by these models is the existence of two large anomalous volumes located at the bottom of the mantle beneath Africa and the Pacific (first reported by Su et al., 1994). These two nearly antipodal reservoirs, usually referred to as Large Low Shear Velocity Provinces (LLSVPs), cover up to 30% of the core-mantle boundary (CMB) and may reach a height up to 1000 km (see review by Garnero et al., 2016, for more details). LLSVPs are characterized by a reduction of both the S-wave (V_S) and P-wave (V_P) velocities by more than 2% and 0.5%, respectively, but an increase in the bulk sound velocity V_ϕ around

2

0.5-1%. This causes an anti-correlation between V_S- and V_ϕ-anomalies (Masters et al., 2000), also observed in normal mode data (Trampert et al., 2004). Early studies have noted that, while a temperature excess may explain the reductions in V_S and V_P, it should also induce a reduction of V_ϕ that is not observed. The anti-correlation between the behavior of V_S and V_ϕ was therefore interpreted as an evidence of the thermo-chemical nature of LLSVPs (Ishii and Tromp, 1999), i.e., these structures differ in temperature and composition from the far-field mantle.

Since their discovery, important efforts have been made to determine the nature and origin of LLSVPs. In particular, several geodynamical studies have explored various possible scenarios that may lead to the formation of structures mimicking LLSVP (Tackley, 1998; McNamara and Zhong, 2005; Nakagawa et al., 2010; Li et al., 2014). A common conclusion of these studies is that a reservoir of material denser than the bulk mantle can explain the shape of LLSVPs. However, it is difficult to estimate precisely the required density excess because other parameters (e.g., rheology) also influence the thermo-chemical structure (Deschamps and Tackley, 2008). In these works, the authors mainly used the shape of the LLSVPs to assess the relevance of their models neglecting the constraints given by the seismic wave speeds anomalies. Alternatively, some studies have used available data from mineral physics to constrain the potential composition of LLSVPs (Samuel et al., 2005; Deschamps et al., 2012). More specifically, they calculated the density and seismic wave speeds for a large range of compositions and compared them to seismological and geodynamical constraints. They found that a reservoir enriched in bridgmanite ($\sim$ 90 vol%) and iron ($\sim$ 12 – 14 wt%), with respect to a pyrolitic composition, provides a good fit to observations.

Previous studies, however, have left behind several important parameters such as the effects of alumina, ferric-ferrous iron ratios, and spin state transition. Here, we use a model including these effects, together with an updated database for the properties of minerals, to investigate the ability of about 81 millions thermo-chemical models to

explain the seismic signature of LLSVPs. Our mineralogical model is characterized by six free parameters that are allowed to vary in large ranges: phase proportions in the mineralogical assemblage (bridgmanite, Ca-silicate perovskite, and ferropericlase, which is dependent on the previous two as their sum must be 100%), iron and aluminium content in that assemblage, ferric/ferrous iron ratio in bridgmanite (the only phase hosting iron in those two valence states), and temperature. For each set of parameters, the density and seismic wave speed anomalies are calculated using the Mie-Grüneisen-Debye equation of state. The incorporation of alumina in bridgmanite changes its bulk modulus, density and the Fe-Mg exchange coefficient between bridgmanite and ferropericlase (Catalli et al., 2011; Piet et al., 2016; Shukla et al., 2016), while spin state transition affects mainly the density and bulk modulus of ferropericlase (Fei et al., 2007; Catalli et al., 2010). As a consequence, these new features induce important modifications on the calculated properties. For instance, a much higher content of FeO can be incorporated (up to 25wt%) without leading to excessively high density.

The identification of plausible thermo-chemical models requires to compare our results with observations. Generally, available seismic observations provide robust constraints on the seismic wave speed anomalies of LLSVPs. We therefore calculate these anomalies by comparing the seismic wave speeds obtained for the different thermo-chemical models considered, with the ones obtained for a typical composition and pressure-temperature conditions of the bulk lower mantle. The calculated anomalies are then compared to the observed ones. Due to uncertainties, we consider as successful all the cases with: (i) V_S-anomalies between -2% and -7%; (ii) V_P-anomalies lower than -0.5%, both being based on seismic tomography observations (e.g., Houser et al., 2008; Koelemeijer et al., 2016); (iii) positive V_ϕ anomalies, for example observed in normal mode data (Trampert et al., 2004); (iv) compositional density (ρ) increase between 2% and 2.8%, based on the values required by geodynamical studies to produce reservoirs with the shape of LLSVPs (Li et al., 2014). From all the models we tested,

a collection of 79000 cases, involving a large range of properties, satisfies these constraints. We then describe and discuss in details these successful compositions.

2. Mineralogical model of the lower mantle

In order to calculate the density and seismic wave speed anomalies of LLSVPs, it is first necessary to know the properties of the bulk (far-field) mantle. In this section, we provide its general characteristics and the method used to calculate its density and seismic wave speeds. This process is based on an approach similar to that of Vilella et al. (2015).

2.1. General description of the reference composition

Our (reference) pyrolitic composition is composed of 18 vol% ferropericlase (Mg,Fe)O (hereafter called Fp), 75 vol% Bridgmanite (Mg,Fe)(Al,Si)O_3 (hereafter called Bm), and 7 vol% Ca-silicate perovskite CaSiO_3 (hereafter called CaPv). The assemblage contains 8 wt% FeO and 3.6 wt% Al_2O_3 to stick to a primitive mantle composition (e.g. McDonough and Sun, 1995). We further assume that iron in bridgmanite is 50% ferric and 50% ferrous, i.e., an oxidation state $Fe^{3+}/\sum Fe$ equal to 0.5. The Fe-Mg exchange coefficient between Bm and Fp,

$$K^{\text{Bm-Fp}} = \frac{\left(\dfrac{\text{Fe}}{\text{Mg}}\right)_{\text{Bm}}}{\left(\dfrac{\text{Fe}}{\text{Mg}}\right)_{\text{Fp}}}, \tag{1}$$

is assumed to be constant and equal to 0.5 (Piet et al., 2016). Using this value, combined with the assumed FeO content, we can obtain the proportion x_{fp} of FeO in ferropericlase, $(1 - x_{fp})$MgO-(x_{fp})FeO, and the proportion x_{Bm} of iron in Bm (Supplementary Material). To determine the proportion of the different components in Bm, we assume that ferrous iron enters into Bm as FeSiO_3, while ferric iron enters into Bm as FeAlO_3. If there is an excess of Fe^{3+}, Fe_2O_3 enters into Bm, whereas if there is an

5

excess of Al, Al_2O_3 enters into Bm. Finally, we include the effect of the Fe^{2+} spin state transition in ferropericlase following Vilella et al. (2015). A more detailed description of the model is available in Supplementary Material.

2.2. Density of the rock assemblage

We first estimate the isothermal bulk modulus at ambient conditions K_{T0} of pure end-members assuming a Voigt-Reuss-Hill average and using measurements of poly-crystal (Supplementary Table 1). Using these derived values combined to the proportion of the different components (described in section 2.1 and Supplementary Material), we calculate the K_{T0} of the three minerals assuming again a Voigt-Reuss-Hill average. We then use the Mie-Grüneisen-Debye equation of state (Jackson and Rigden, 1996) to calculate the ratio V_0/V (or equivalently ρ/ρ_0) of each mineral,

$$
\begin{aligned}
P = \frac{3K_{T0}}{2} &\left[\left(\frac{V_0}{V} \right)^{7/3} - \left(\frac{V_0}{V} \right)^{5/3} \right] \\
&\left\{ 1 - \frac{3}{4}(4 - K'_{T0}) \left[\left(\frac{V_0}{V} \right)^{2/3} - 1 \right] \right\} + \Delta P_{th},
\end{aligned}
\tag{2}
$$

where ΔP_{th} is the thermal pressure and the subscript zero indicates ambient conditions for volume V_0, temperature T_0, isothermal bulk modulus K_{T0} and its pressure derivative K'_{T0}. Values used for mineral properties are reported in Supplementary Table 1 and 2. To obtain the density (ρ) of each mineral we now only need to calculate their density at ambient conditions (ρ_0). For this, we estimate V_0 for each mineral following a procedure similar to that for K_{T0}, except that we use a simple arithmetic mean instead of a Voigt-Reuss-Hill average. Finally, the density of the rock assemblage is obtained by calculating the arithmetic mean of the density for the three minerals considered.

2.3. Seismic wave speed of the rock assemblage

The calculation of the bulk sound speed,

$$
V_\phi = \sqrt{\frac{K_s}{\rho}},
\tag{3}
$$

requires only the determination of the isentropic bulk modulus K_s that can be obtained from the isothermal bulk modulus K_T,

$$K_s = K_T(1 + \alpha\gamma T),\tag{4}$$

where α is the thermal expansion coefficient and γ the Grüneisen parameter. All the parameters in the eq. 4 can be calculated using the formalism of the Mie-Grüneisen-Debye equation of state(see Supplementary Material for more details), so that the calculation of V_ϕ is straightforward.

The determination of V_S and V_P is however more complicated because they further depend on the shear modulus (G),

$$V_S = \sqrt{\frac{G}{\rho}}, \qquad V_P = \sqrt{\frac{K_s + (4/3)G}{\rho}}.\tag{5}$$

We calculate G in two steps. First, we use an available equation of state to account for the pressure dependence (e.g., Bina and Helffrich, 1992),

$$G(T = 300\ K, P) = \left(\frac{V_0}{V}\right)^{5/3}\left[G_0 + 0.5\left[1 - \left(\frac{V_0}{V}\right)^{2/3}\right]\left(5G_0 - 3G_0'K_{T0}\right)\right],\tag{6}$$

with G_0 and G_0' being the shear modulus and its pressure derivative at ambient conditions. Second, the temperature dependence is calculated following,

$$G(T, P) = G(T = 300\ K, P) + dG/dT(T - 300),\tag{7}$$

where dG/dT is the temperature derivative of the shear modulus. Values of dG/dT are given by laboratory experiments, while values of G_0 and G_0' are estimated using measurements of polycrystal following a similar procedure that for the isothermal bulk modulus (Table 1).

It is important to note that the determination of the shear modulus is subject to much

larger uncertainties than the determination of the density and bulk modulus. First, the experimental measurements are more challenging. Less data are available, and measurements are less robust. As such, we also consider results from ab-initio calculations for the shear modulus of Al-bearing bridgmanite (Shukla et al., 2015, 2016). Second, eqs. 6 and 7 used to extrapolate measurements are also less accurate. In particular, we use the temperature derivative of the shear modulus to estimate its temperature dependence (eq. 7), while it is likely to induce large uncertainties, since this temperature derivative is probably not constant with pressure (Shukla et al., 2016).

The procedure developed here allows to calculate the density, S-wave velocity, P-wave velocity and bulk sound speed as a function of pressure and temperature. The results for our reference composition are displayed in Supplementary Material. Interestingly, the same procedure can be applied to a large diversity of compositions, especially to compositions that may be relevant for LLSVPs. In the following section, we describe all the potential compositions investigated, with a particular emphasis on those explaining the seismic signature of LLSVPs.

3. Potential compositions of LLSVPs

3.1. Range of compositions investigated

The purpose of this work is not to test specific LLSVPs compositions or natures, but to follow an approach with no preconception on their compositions. However, it is in practice impossible to consider all the minerals that potentially exist at the bottom of the mantle. The compromise proposed here is to focus only on rock assemblages consisting of the three minerals expressed in a pyrolitic composition (Bm, CaPv, Fp), while varying all compositional parameters within this assemblage. By varying the proportions of SiO_2, MgO, CaO, Al_2O_3, and FeO, we can vary the phase proportions of Bm, CaPv, and Fp, as well as the iron and aluminium content in these phases along with the oxidation state. For the sake of simplicity, we chose to describe these compositional

parameters as the volumetric phase proportions of Bm and CaPv (Fp is bound to the others as the sum Fp+Bm+CaPv has to be 100%), Al_2O_3 content which is incorporated in Bm, FeO content which partitions between Bm and Fp according to the partition coefficient (Eq. 1), and the oxidation state ($Fe^{3+}/\sum Fe$ in Bm). Each of these parameters is varied in a systematic way within the lower and upper bounds listed in Table 2.

Finally, we prescribed the pressure and temperature conditions relevant for both the far-field mantle and LLSVPs. We consider a far-field mantle with a pressure of $P =$ 130 GPa, corresponding to the lowermost mantle, and a temperature of $T = 3000$ K. For the sake of simplicity, the same pressure P is considered for LLSVPs, while, because LLSVPs temperature is unknown (and likely to vary laterally), we allow their temperature $T + \Delta T$ to vary. The temperature contrast (ΔT) between far-field mantle and LLSVPs stands as the sixth parameters of our model (Table 2). In the following, this six-dimensional space is sampled uniformly giving an ensemble composed by more than 81 millions models to investigate.

3.2. Influence of explored parameters on seismic properties

Before identifying and discussing potential compositions of LLSVPs, it is important to characterize the effects of the six parameters on density and seismic wave speeds. Because of the relatively large number of models and input parameters, we mainly present results using 2D histograms showing the distribution of all models as a function of one input parameter and one output (V_P, V_S, V_ϕ, ρ). The main interest of these histograms is to reveal the trends between input parameters and outputs. Narrow distributions and large variations indicate that the input parameter is likely the dominant parameter affecting the output. By contrast, wide distributions without clear variations suggest that the input parameter does not substantially affect the output. We plotted the 2D histograms for each output as a function of all 6 parameters. Figure 1 shows the histograms corresponding to the dominant parameters (other histograms are shown in Supplementary Material).

9

The V_S anomaly is dominantly affected by the temperature contrast, with decreasing V_S as the temperature contrast increases. Note that the V_S anomaly decreases by about 1% for only a 200 K increase, which stands as a very strong effect. The Al_2O_3 content also plays a role, with a ~2% decrease of V_S for a 10wt% increase of the Al_2O_3 content. However, large change in Al_2O_3 content is required to impact V_S, so that temperature variations appear to be a more straightforward mechanism to produce V_S anomalies in the lower mantle. The V_P anomaly exhibits a similar behavior as the V_S anomaly, except that the Al_2O_3 content has a slightly larger impact than temperature. The V_ϕ anomaly is mainly affected by the Al_2O_3 content, with V_ϕ decreasing as Al_2O_3 content increases, and to a lesser extent by the oxidation state with V_ϕ increasing with $Fe^{3+}/\sum Fe$. Finally, density is, as expected, mainly affected by the FeO content, with increasing ρ as FeO content increases.

From a more general perspective, one may note that the three seismic wave speeds exhibit similar behaviors with variations of input parameters (Supplementary Figure 2–4). In particular, seismic wave speeds are decreasing with increasing FeO content. The effects of the temperature contrast and FeO content are therefore in agreement with the findings of previous studies (Samuel et al., 2005; Deschamps et al., 2012). Perhaps more surprising is the nonlinear effect of the Al_2O_3 content (figure 1). For Al_2O_3 content up to 4 wt%, seismic anomalies slightly increases and decreases for larger contents. This nonlinear effect shows that it may not be fully appropriate to consider a constant seismic sensitivity throughout the explored parameter range as it has been done for simpler mineralogical compositions (Deschamps et al., 2012). Finally, we note that the FeO contents investigated here (up to 28wt%) are much higher than in previous studies (up to 14wt%). Our results suggest that adding Al_2O_3 in the composition changes importantly the properties of the rock assemblage and allows to incorporate a much larger proportion of iron while maintaining a reasonable density. The incorporation of alumina is therefore crucial to investigate realistic mantle compositions and to obtain

more robust results.

3.3. Constraints on LLSVPs

It is difficult to determine unambiguously the precise characteristics of LLSVPs. First, these properties are likely to vary laterally, because of lateral variations of temperature and composition (Ballmer et al., 2016). Second, different tomographic models suggest different properties depending on the dataset and methods used. Third, tomographic models are generally obtained through a linearized and regularized inversion that includes damping and smoothing, so that the actual seismic signature of LLSVPs may be underestimated.

As a consequence, we choose here to select compositions satisfying rather conservative conditions:

- V_S anomaly compared to the far-field mantle between -7% and -2%.

- V_P anomaly compared to the far-field mantle lower than -0.5%.

- Positive V_ϕ anomaly compared to the far-field mantle.

Note that constraining the V_ϕ anomaly is challenging because it relies on the determination of V_S and V_P that are usually imaged with separate tomographic inversions at different resolution and with different levels of uncertainties. Nevertheless, seismic tomography (Masters et al., 2000; Houser et al., 2008) and normal mode data (Ishii and Tromp, 1999; Trampert et al., 2004) suggest a positive anomaly. We thus follow a conservative approach by applying this condition without setting an amplitude for the anomaly. In addition to these seismic constraints, we also use geodynamical constraints and restrict our study to models with a compositional density difference between 2% and 2.8% compared to the far-field mantle. This condition is suggested by the density difference required to produce chemically distinct reservoirs with the shape of LLSVPs in geodynamic models (e.g., Li et al., 2014). For lower compositional density differences, the material is entrained and mixed by mantle convection so that reservoirs are

not stable. For larger compositional density differences, gravity segregation occurs and reservoirs tend to form layers without large topography. Among the ~81 millions models studied, only about 79000 satisfy these conditions. Figure 1 suggests that most of cases are compatible with the V_P and V_S anomalies deduced from seismic observations. Hence, constraining potential compositions of LLSVPs requires constraints on V_ϕ and ρ. Interestingly, as discussed in section 3, our calculation of V_ϕ and ρ is much more robust than of V_P and V_S. Therefore, uncertainties on the determination of the shear modulus, and thus on V_P and V_S, do not affect significantly our results. Note that from a seismological point of view, it is the opposite, since V_P and V_S are much better constrained than bulk velocity and density. In the remainder of this study, we focus on the 79000 successful models. Note that the properties of these models are available for academic purposes (Vilella, 2020).

3.4. Characteristics of LLSVPs

The 1D and 2D-histograms showing the distribution of the successful models are reported in figure 2 for the six parameters. It is important to note that these distributions are not indicative of the probability of a composition to explain LLSVPs, as changing the sampling of the input parameters (i.e., lower and upper bounds) may change substantially the observed distributions. Moreover, the sampling of the parameter space is intrinsically uneven because of the overall decreasing number of possible composition with increasing proportion of Bm. A simple way to explain this is that in the extreme case of 100% of Bm, CaPv is of course absent, whereas for a proportion of Bm equal to 60%, the proportion of CaPv+Fp is equal to 40%, so that the proportion of CaPv can take any values between 0 and 40%. This uneven sampling tends to increase the frequency of occurrence for low proportion of Bm or CaPv. It is therefore important to focus only on the trends between the different parameters and on the conditions for which no successful composition have been found, which are both robust features.

A thorough analysis of the results is however difficult because of the large number

of parameters and successful models. To overcome this issue, we can try to reduce the number of parameters by identifying existing trade-offs. For instance, there is a strong anti-correlation between the proportion of Bm and CaPv (figure 2), i.e., an increase in the proportion of Bm have to be balanced by a decrease in CaPv (and vice versa). More specifically, figure 2 shows that the proportion of Fp should remain almost constant and is typically <6%, i.e., LLSVPs should be characterized by a much lower proportion of Fp than the far-field mantle. Because Fp has a lower V_ϕ than other minerals, higher proportions of Fp are characterized by a negative V_ϕ anomaly, in contradiction with available constraints, and are therefore unlikely. Furthermore, this anti-correlation also suggests the existence of a linear relationship between the proportion of Bm and CaPv, i.e., these two parameters are not independent and one of them can be chosen as a representative for the two. In order to identify and quantify all the existing trade-offs, we apply a principal component analysis (PCA) to our dataset.

3.4.1. Principal Component Analysis

The PCA provides a projection of a dataset in a new orthogonal coordinate system where the vectors, called components, are linear combinations of the input parameters. In this approach, the new vectors are successively built such that they best explain the variability of the dataset. The relative importance of each component is given by their corresponding eigenvalue. If one or several eigenvalues are much lower than others, then all the variability can be explained by a lower number of parameters, indicating the existence of one or several trade-offs between the input parameters. The components with a high eigenvalue can be analyzed to highlight the underlying trade-offs, and in turn reduces the number of independent parameters. The six components of our dataset with their eigenvalues are reported in Table 3. Because the eigenvalues 1-3 are much higher than the eigenvalues 4-6, the components 4-6 can be viewed as negligible and the components 1-3 are the principal components. The dimension of our parameter space can therefore be reduced from 6 to 3 independent parameters. To verify this, we

13

plotted our dataset in the orthogonal system formed by the eigenvectors 1-3 (figure 3). In this coordinate system, the distributions do not exhibit any trade-offs confirming that all the information have been extracted by the PCA. We now conduct a detailed analysis of the principal components in order to identify these trade-offs.

The first component is dominated by the opposite contribution from the proportion of Bm (0.600) and CaPv (-0.591). Note that, although weaker, a similar behavior can be observed in the components 2 and 3. This corresponds to the anti-correlation between CaPv and Bm discussed in section 3.4. The second component is dominated by the contribution of the Al_2O_3 content and oxidation state, while the temperature contribution is also significant. By comparing the three principal components, one may see that the FeO content, Al_2O_3 content and oxidation state are always correlated. These correlations can also be seen from the 2D-histograms displayed in figure 2 and from the end-members identified in figure 3. Interestingly, these three elements are required to form the $FeAlO_3$ component in Bm. We therefore postulate that the $FeAlO_3$ component in Bm has a better ability to explain observations than other iron-bearing components, which causes a robust correlation between the FeO content, Al_2O_3 content and oxidation state. To support this point, we have verified the low proportion of Al_2O_3 and Fe_2O_3 components in all the successful cases (see Supplementary Figure 5). Furthermore, increasing the proportion of the $FeAlO_3$ component has the direct effect of increasing density. This component may thus be interpreted as a density shift vector, while the third component affects mainly the temperature.

From the analysis of the end-members in figure 3 and the principal components, we postulate that all the successful cases can be separated in two end-member compositions: one CaPv-rich and one Bm-rich. For both composition, we applied a PCA and found the same trade-offs as for the full set of successful models, e.g., the correlation between FeO content, Al_2O_3 and $Fe^{3+}/\sum Fe$. We now study in more detail these two end-member compositions beginning with the Bm-rich case.

14

3.4.2. End-member composition: Bm-rich

Building on the results of the PCA, we apply an additional condition to our success-ful models, that is the Bm proportion should be larger than 90vol%. The purpose of this condition is to extract the Bm-rich end-member composition from the tally of success-ful models. We have selected this specific proportion because it is high enough to be restrictive, while providing a number of cases (~9000) sufficient for the data analysis. In the following, the results are displayed using histograms of the successful models as a function of two input parameters. As suggested by the PCA, we focus on the effect of ΔT and the FeO content, which can be viewed as a representative parameter for the Al_2O_3 content and oxidation state.

Figure 4a shows the distribution of the Bm-rich models as a function of ΔT and FeO content. For these models, a large range of temperature is possible, while larger temperatures seem slightly more likely for FeO content ~21wt%. Although not fully robust, observations may be easier to explain with temperature contrast lower than 500 K. FeO contents are typically >14wt% with values up to 25wt%. As predicted, Al_2O_3 content (typically >8wt%, not shown here) and oxidation state (typically larger than 0.6, not shown here) are also high. Compositions more enriched in Bm seem to slightly favor larger FeO contents, Al_2O_3 contents and oxidation states while involving slightly lower temperature contrasts.

3.4.3. End-member composition: CaPv-rich

We follow a similar procedure for the CaPv-rich end-member composition by se-lecting only the successful cases with a proportion of CaPv larger than 30vol%. A total of 32000 cases was obtained from the 79000 initial successful cases. The main results are displayed in figure 4b. As for the Bm-rich case, a wide range of temperature is pos-sible, but observations seem easier to explain with a temperature contrast lower than 500 K. Note that the distribution is now slightly more scattered than in the Bm-rich case and does not exhibit any specific trend with increasing proportion of CaPv, this result

being valid for all the parameters. The FeO content is typically between 10wt% and 21wt%, the Al_2O_3 content between 3wt% and 13wt%, and the oxidation state larger than 0.3.

4. Discussion

4.1. Summary of the results

We investigated a large range of models for LLSVPs with varying FeO content, Al_2O_3 content, proportion of CaPv, proportion of bridgmanite, oxidation state $Fe^{3+}/\sum Fe$, and temperature contrast with respect to the far-field mantle ΔT. We found that constraints on density and bulk sound speed of LLSVPs are by far the most useful observations to identify the potential composition of these structures. By contrast, the low V_S and V_P observed are easily achieved as long as LLSVPs are a few hundreds Kelvin hotter than the far-field mantle. Two robust results are that the proportion of Fp should be low (<6vol%), and that the formation of Fe^{3+}-bearing bridgmanite is much more favorable than other iron-bearing components. As a consequence, we observed a clear trade-off between FeO content, Al_2O_3 content and $Fe^{3+}/\sum Fe$. To describe the large number of models, we identified two end-member compositions: one Bm-rich and one CaPv-rich. For each end-member, a large range of temperature is possible, although it seems easier to explain seismic observations with low temperature contrasts (<500 K). Furthermore, we found fairly high FeO and Al_2O_3 content, up to 25wt% and 19wt%, respectively. It is important to note that a full range of compositions is possible between these two end-members, so that, from a more general perspective, a very large range of parameters is possible for LLSVPs. Interestingly, temperature excess deduced from normal modes data (Trampert et al., 2004) and attenuation (Deschamps et al., 2019) are in good agreement with our findings, while the high Al_2O_3 content is consistent with the super-chondritic Ca/Al ratio measured for the accessible Earth (e.g., Walter et al., 2004).

4.2. Limitations and potential developments

4.2.1. Effects of post-perovskite

Our results rely on the selected lower mantle mineralogy and on the thermo-elastic properties of these minerals. More specifically, other minerals that the three used in our model may be present in the lowermost mantle. In particular, we did not account for the possible presence of post-perovskite (PPv, see Shim, 2008, for a review), a high-pressure phase of bridgmanite. PPv is characterized by a slightly higher density, lower bulk sound speed, and higher shear-wave speed than Bm (see Cobden et al., 2015, for a compilation), such that its presence outside LLSVPs has been advocated as an explanation for the anti-correlation between V_ϕ and V_S-anomalies (e.g., Davies et al., 2012). A difficulty, however, is to precisely determine the stability field of PPv, which depends on temperature and pressure (e.g., Catalli et al., 2009), but also on the amount of iron and alumina (e.g., Sun et al., 2018). In particular, the transition pressure increases with increasing temperature and decreasing alumina and iron content. Because of these dependencies, and following the assumed conditions and composition, PPv may or may not be present in the lowermost mantle. In our case, the assumed far-field mantle is likely composed of a mixture of Bm and PPv. If only the thermal effect is accounted for, the transition pressure of PPv should be too large to occur within LLSVPs. However, if LLSVPs are strongly enriched in alumina and iron, the transition pressure of PPv may be smaller than the CMB pressure (Sun et al., 2018), i.e., PPV may be stable within LLSVPs. In that case, PPv may be present both outside and within LLSVPs, such that its seismic signature would be reduced. Unfortunately, available constraints concerning the effects of alumina and iron content on the properties of PPv are too scarce to allow a careful estimate of its effects.

4.2.2. Uncertainties

Although our reference composition is compatible with available constraints (see Supplementary Material), the precise composition of the far-field mantle remains un-

certain. The uncertainties that may affect our reference composition should therefore be properly addressed. In that aim, we have investigated the impact of compositional variations in our reference composition. The results show that changing the reference composition shift the range of possible compositions for LLSVPs. For instance, increasing (decreasing) the proportion of Fp in the reference composition induces an increase (decrease) of the maximum proportion of Fp in the range of possible compositions for LLSVPs. Nevertheless, we found that the modification of the reference composition does not impact the main conclusions of our work. The proportion of Fp in LLSVPs has to be lower than in the reference composition, while the formation of Fe^{3+}-bearing bridgmanite is favored over other iron-bearing components. Furthermore, there are uncertainties on the exact value of mineral properties, especially concerning the shear modulus, as contrasted results have been found for the elasticity of Fp (Murakami et al., 2012; Wu et al., 2013). These uncertainties may impact our results. As a matter of fact, using the ab-initio results of Wu et al. (2013), instead of the experimental results of Murakami et al. (2012), leads to LLSVPs with a maximum proportion of Fp that is slightly higher (from ~6% to ~8%).

Overall, this supports our methodology relying on the identification of the general trends in the potential composition of LLSVPs, rather than on the search of the most probable composition. Since both the unknown parameters and observations are defined as relative to a reference lower mantle, an error in the reference mantle will only produce a bias (e.g. a systematic error) in our results. Therefore, all the relative information between inferred parameters (trade-offs, and relative compositions) are robust features that remain mostly unaffected by reasonable uncertainties on the reference composition.

4.2.3. Additional constraints

One way to reduce the range of plausible thermo-chemical models for LLSVPs is to use tighter constraints. Improvement in tomographic models, leading to a precise es-

timate of the V_ϕ anomaly, would reduce the range of possible compositions. Additional constraints may also be useful. For instance, tidal tomography (Lau et al., 2017) provides a constraint on the effective density difference ($\Delta\rho_{tot}$), i.e., including the thermal and compositional effects, between LLSVPs and the far-field mantle. Using a simple model of the lower mantle composed of three 340 km thick layers, Lau et al. (2017) found that LLSVPs should be ~0.60% denser. In comparison, the minimum $\Delta\rho_{tot}$ of our successful cases is slightly larger, at ~ 1%. This discrepancy may be related to the underestimation of $\Delta\rho_{tot}$ in tidal tomography models due to a dilution effect, or may be indicative of a lower density difference between LLSVPs and far-field mantle than the one assumed in this work. In both cases, constraining the effective density difference stands as a very robust way to infer the nature and composition of LLSVPs. Supplementary constraints may further include seismic attenuation. Assuming that seismic attenuation is mainly affected by temperature, it can be used to constrain the temperature conditions of LLSVPs (Deschamps et al., 2019). Although it may be affected by several sources of uncertainties, it is interesting to note that in the western tip of the Pacific LLSVP, modeling of attenuation predicts a temperature excess of 350 +/- 200 K (Deschamps et al., 2019), a value consistent with the temperature excess suggested by our calculations. A better knowledge of mineral properties may refine the modeling of attenuation, allowing sharper constraints on the potential composition of LLSVPs, and therefore the exploration of more complex and detailed mineralogical models. Alternatively, and as illustrated in the next section, the range of potential compositions may be reduced by considering the potential process that created these LLSVPs, and whether the produced compositions are reasonable.

4.3. Potential origin of LLSVPs

4.3.1. The magma ocean hypothesis

Some authors have postulated that the final stages of the solidification of a primitive magma ocean could be the source of LLSVPs (e.g., Labrosse et al., 2007; Ballmer

et al., 2017). However, the potential composition produced by such a scenario remains largely uncertain, mainly because the solidifying process itself is uncertain (see Solomatov, 2015, for more details). First, different modes of crystallization are possible that may or may not produce chemically distinct reservoirs. Second, the sequence of crystallization is highly debated and depends, in particular, on the relative behavior of the adiabatic temperature gradient and the liquidus profile (e.g., Boukaré and Ricard, 2017), which, again, is uncertain at lower mantle conditions (Andrault et al., 2011; Nomura et al., 2011). Moreover, depending on the value of the iron partitioning coefficient between solid and melt, the crystals could be denser than melt or not (Nomura et al., 2011; Andrault et al., 2012; Tateno and Hirose, 2014; Caracas et al., 2019). Considering all these uncertainties, the magma ocean could solidify from the bottom and propagate to the surface (bottom-up scenario), or from the middle and propagate to both the surface and the CMB (middle-out scenario). In the latter case, a basal magma ocean (BMO) is produced that may give birth to LLSVPs (Labrosse et al., 2007). In the bottom-up scenario, the dense reservoir is located near the surface and should overturn to produce a stable density gradient (Elkins-Tanton et al., 2003), potentially producing a basal magma ocean (Ballmer et al., 2017).

Independently of the solidification scenario, the residual liquid should be enriched in iron and alumina (Tateno and Hirose, 2014; Boujibar et al., 2016). A first order estimate of such an enrichment can be obtained using the simplified model proposed by Boukaré et al. (2015, 2018). In this model, the Nerst partition coefficient D between melt and solid is assumed to be constant so that,

$$C_s = C_{s,0}D\left(\frac{R_{min}^3 - R_{max}^3}{R_{min}^3 - R^3}\right)^{1-D}, \tag{8}$$

where C_s is the proportion of the element in the solid, $C_{s,0}$ the initial proportion, R_{max} the Earth's radius, R_{min} the CMB radius, R the radius considered. Considering that LLSVPs originate from a layer 300 km thick, we obtained a FeO content of about

28wt% for $D = 0.6$ and above 50wt% for $D = 0.4$. A reasonable FeO content can therefore only be obtained for $D > 0.5$, which may require a low degree of melting (Boujibar et al., 2016). For such low degrees of melting, alumina may be partitioned equally between melt and solid (Boujibar et al., 2016). This stands in contradiction to the alumina enrichment suggested by our results. Furthermore, if we consider a thinner magma ocean (~1000 km), this constraint is somewhat relaxed, but still requires low degrees of melting (<10%) that seems unrealistic for the slow-cooling basal magma ocean. Another possible issue is the oxidation state of the magma ocean, which should be initially fairly low. However, FeO-disproportionation may induce a progressive increase of the oxidation state during the crystallization.

Alternatively, in the bottom-up scenario, the dense reservoir (highly enriched in FeO) could undergo partial melting during its overturn (Ballmer et al., 2017). The subsequent melt-rock interactions may alter the composition of the dense reservoir, decreasing its FeO content while increasing its Al_2O_3 and SiO_2 contents. Overall, since the style of magma-ocean freezing is poorly constrained, and element partitioning at high pressures is difficult to measure, it remains challenging to estimate precisely the composition of the produced reservoirs.

Another way to evaluate the relevance of the magma ocean origin is by looking at mineral proportion. It has been suggested that Bm is the first mineral to crystallize, followed by Fp and CaPv (Tronnes and Frost, 2002). In that case, the residual liquid of magma ocean should be enriched in CaPv and, to a lesser extent, in Fp. However, our results suggest that a low proportion of Fp (~6vol%) is required to explain the seismic signature of LLSVPs. Therefore, if we further assume that the produced reservoirs should not be significantly altered during the Earth's evolution, these reservoirs should be highly enriched in SiO_2 to prevent the formation of Fp. If one assumes that LLSVPs are related to magma ocean solidification, then an additional process (e.g., Ballmer et al., 2017; Hirose et al., 2017) is required to explain the depletion in Fp. As a conse-

quence, we propose that the low proportion of Fp may be a more robust constraint than the FeO content to confirm or not the magma ocean origin for LLSVPs.

4.3.2. The MORB hypothesis

Another possible origin for LLSVPs is the accumulation of MORB materials. At lower mantle conditions, MORB is believed to be composed of ~20vol% of CaPv, ~40vol% of Bm and other phases, such as calcium ferrite-type phase, accounting for the remaining ~40vol% (Ricolleau et al., 2010). In addition, MORBs cover a large compositional range (Gale et al., 2013), including substantial differences in the amount of FeO, and may further be chemically altered during subduction and related metasomatism. Due to this strong dispersion in composition, the density and seismic signature of recycled MORBs are still debated. For instance, numerical simulations of mantle convection (Nakagawa et al., 2010) indicate that this dispersion may affect the ability of MORBs to accumulate at the CMB, as their density contrast with respect to the far-field mantle strongly depends on their FeO content. Taking into account the compositional dispersion to estimate the seismic signature of high pressure MORBs, Deschamps et al. (2012) noted that LLSVPs may not be entirely composed of recycled MORB, unless their temperature exceeds that of the far-field mantle by 1500 K or more. Recent ab initio calculations (Wang et al., 2020) further pointed out that at lowermost mantle conditions, MORBs are characterized by high seismic velocities contrasting with the seismic signature of LLSVPs. However, it cannot be excluded that LLSVP incorporate a small or moderate amount of MORB mixed with primitive material, as assumed in the Basal Melange (BAM) hypothesis (Tackley, 2012; Ballmer et al., 2016). In addition, MORB can undergo melting in the subduction channel inducing a fertilization of the mantle wedge and the production of moderately-enriched mafic lithologies, which may contribute to LLSVPs. Interestingly, experimental results on CaPv (Thomson et al., 2019) are consistent with LLSVPs moderately enriched in recycled MORBs. Because the compositions investigated here do not include all the

22

minerals present in MORBs and have lower SiO_2 contents, our results are not able to evaluate the hypothesis that LLSVP are entirely or partially composed of recycled MORBs.

4.3.3. *The primitive crust hypothesis*

Based on geochemical evidences, Tolstikhin and Hofmann (2005) suggested that the subduction of a primitive crust produced just after the magma ocean solidification could be at the origin of LLSVPs. This primitive crust should be a mixture of komatiitic crust and chondritic regolith, whose proportion and individual composition are uncertain. Nevertheless, we can attempt to verify whether such a mixture could be compatible with our results. Based on lunar regolith composition (e.g., McKay et al., 1991), one may postulate that terrestrial regolith should be enriched in FeO, CaO and Al_2O_3 compared to a pyrolitic composition. Regoliths with a moderate FeO-enrichment (16wt%) are characterized with a reasonable Al_2O_3 content (~13wt%), while FeO-poor regolith (6wt%) are highly enriched in Al_2O_3 (~25wt%). On the other hand, large compositional variations are displayed by komatiites (e.g., Arndt et al., 2008). In particular, some komatiites are characterized by a slight to moderate enrichment in FeO, CaO and Al_2O_3. Using appropriate compositions, we verify that a mixture of regolith and komatiite is compatible with our results. It is however necessary to consider a large proportion of regolith (typically larger than 70%) with moderate FeO-enrichment, otherwise the mixture has a lower FeO content than the ones suggested by our results.

5. Concluding remarks

Using a massive sampling of the parameter space and a principal component analysis, we find that the seismic signature of LLSVPs could be explained as long as the proportion of Fp is low, and that a certain ratio between FeO content, Al_2O_3 content and $Fe^{3+}/\sum Fe$ is maintained. As a result, the seismic signature of LLSVPs can be

explained with a large range of compositions. We thus tried to restrict the range of potential compositions by considering different possible sources for LLSVPs, e.g., solidification of the magma ocean or subduction of a primitive crust. Different scenarios generate reservoirs with a compatible concentration of major elements. However, owing to the lack of constraints available, the mineral proportions of these reservoirs are uncertain. It is therefore difficult to evaluate the relevance of these scenarios.

Table 1: Shear modulus (G_0) along with its pressure (G_0') and temperature (dG/dT) derivative at ambient conditions for several compounds.

Compounds	G_0 (GPa)	G_0'	dG/dT (GPa K^{-1})
Ferropericlase	-	-	-0.02[a]
MgO	131[b]	1.92[b]	-
0.92MgO-0.08FeO (HS)	113[a]	2.15[a]	-
0.92MgO-0.08FeO (LS)	130[a]	2.04[a]	-
Bridgmanite	-	-	-0.02[a]
MgSiO$_3$	168.2[c]	1.79[c]	-
0.875MgSiO$_3$-0.125FeSiO$_3$	165.2[c]	1.80[c]	-
0.875MgSiO$_3$-0.125Fe$_2$O$_3$	143.1[d]	1.88[d]	-
0.875MgSiO$_3$-0.125FeAlO$_3$	156.3[d]	1.83[d]	-
0.875MgSiO$_3$-0.125Al$_2$O$_3$	162.7[d]	1.85[d]	-
CaSiO$_3$	135[e]	1.57[e]	-0.002[e]

[a] Murakami et al. (2012).

[b] Murakami et al. (2009).

[c] Shukla et al. (2015).

[d] Shukla et al. (2016).

[e] Values obtained by fitting the experimental data in Table 8 of Li et al. (2006).

Table 2: Range of values investigated for each compositional parameter considered in our LLSVPs model. The step value indicates the step between 2 adjacent values.

Parameter	min value	step value	max value
FeO content (wt%)	8	1	28
Al_2O_3 content (wt%)	1	0.5	19
Proportion of CaPv (vol%)	0	1	40
Proportion of Bm (vol%)	60	1	100
$Fe^{3+}/\sum Fe$	0	0.1	1
ΔT (K)	0	100	1000

Table 3: Results of the principal component analysis (PCA) applied to our set of successful models. Note that the data have been centered and normalized before analysis, so that the results are here shown in a dimensionless form.

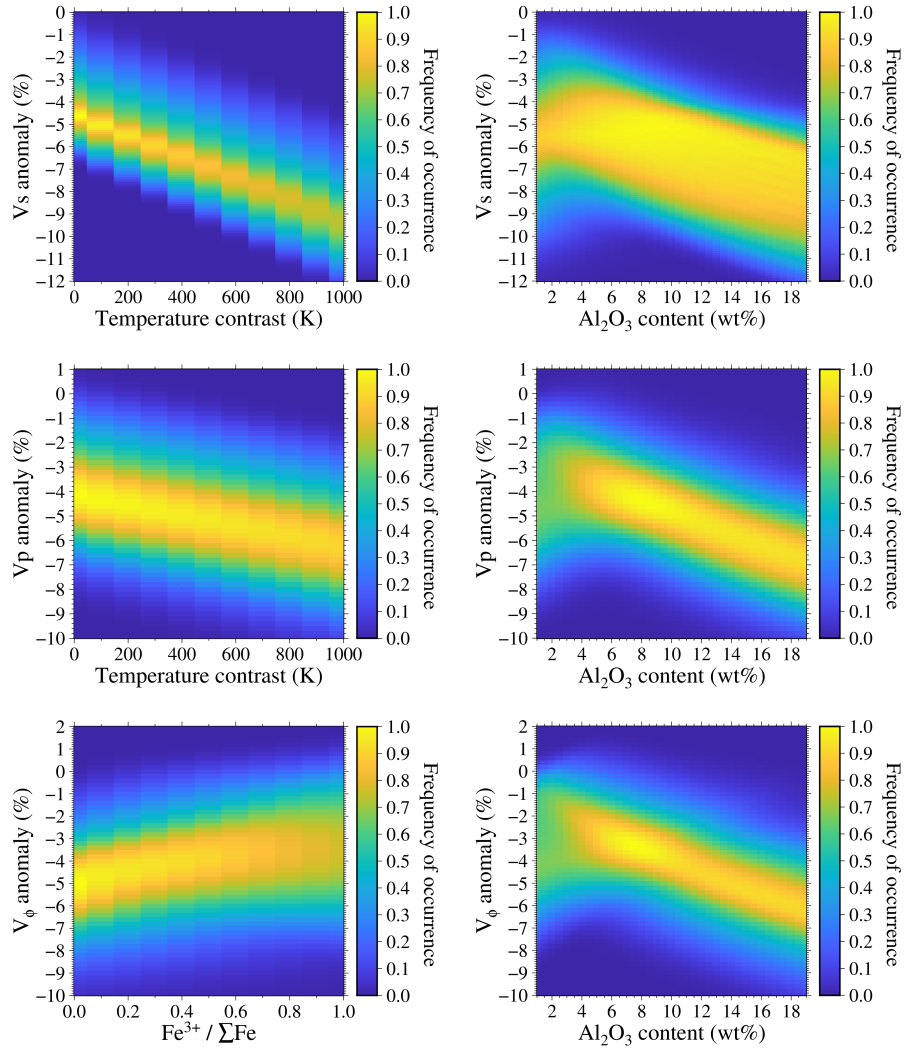|	Components					
	1	2	3	4	5	6
Eigenvalues	0.681	0.296	0.262	0.023	0.003	0.001
Proportion CaPv	-0.591	0.314	-0.187	-0.267	-0.147	0.651
Proportion Bm	0.600	-0.307	0.200	-0.083	-0.255	0.658
ΔT	0.040	0.581	0.813	-0.004	0.008	-0.010
FeO content	0.306	0.217	-0.178	-0.406	0.803	0.137
Al_2O_3 content	0.339	0.395	-0.301	-0.528	-0.518	-0.302
$Fe^{3+}/\sum Fe$	0.283	0.516	-0.377	0.692	-0.012	0.180

Figure 1: 2D histograms showing the distribution of all the models as a function of one input parameter (x-axis) and one output (y-axis). The effect of only two parameters, corresponding to the dominant ones, are reported for each seismic wave speed. Other histograms are shown in Supplementary Material.
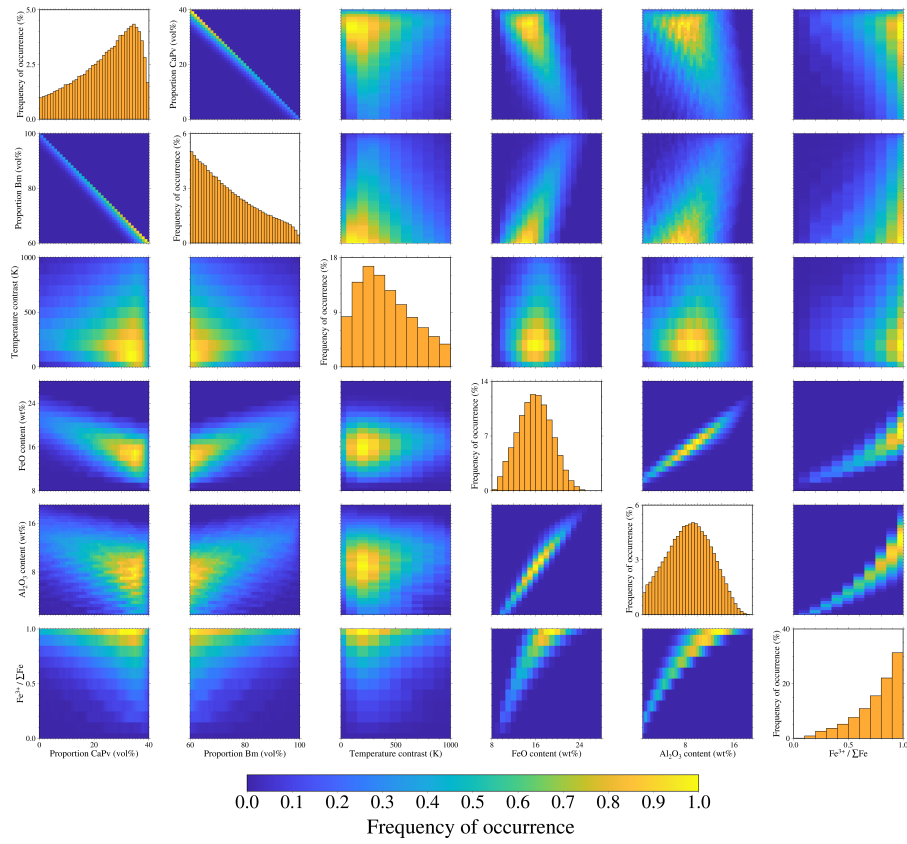
28

Figure 2: Histograms and 2D-histograms showing the distribution of the successful models for all the input parameters (see text for more details).
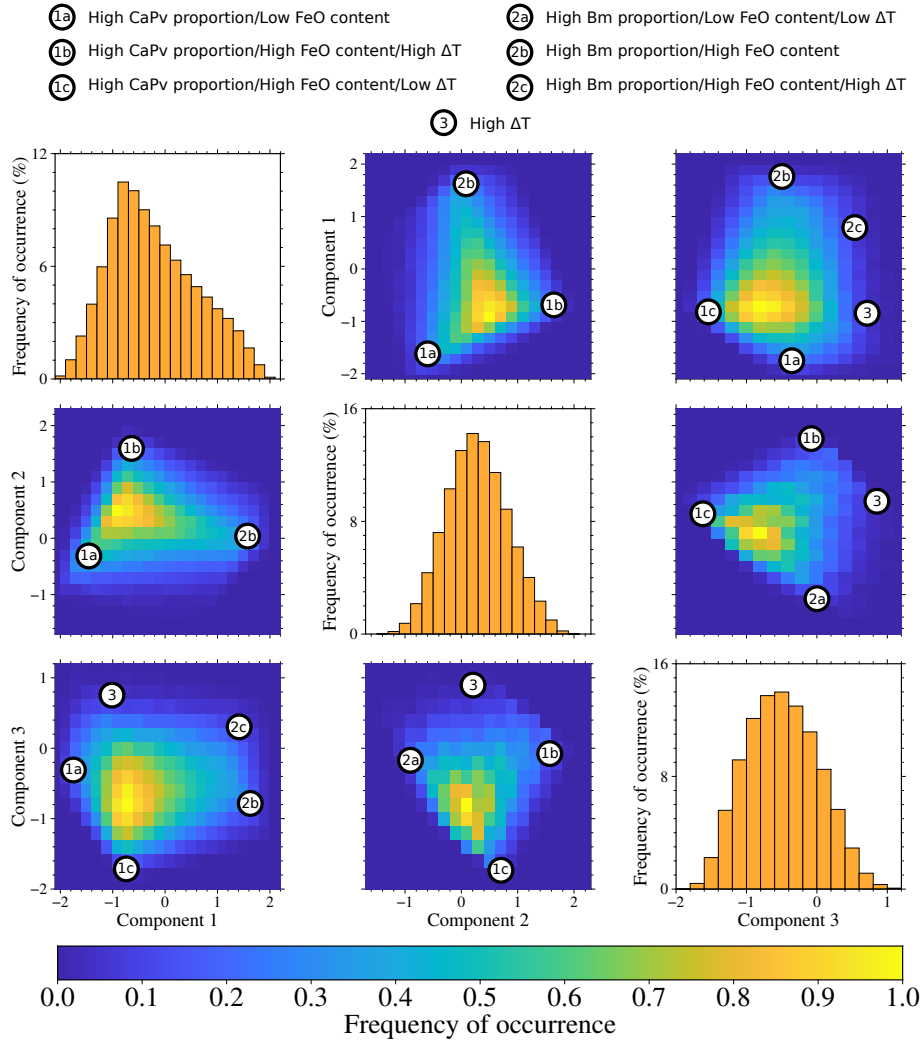
29

Figure 3: Histograms and 2D-histograms showing the distribution of the successful models projected in the principal components space (eigenvectors 1–3 in Table 3). As the principal components space has been centred and normalized, the interpretation of the results requires a rescaling. We therefore provide (above the figure) the characterization of the different end-members cases shown by the 2D-histograms. Note that high CaPv proportions are associated with low Bm proportions (and vice versa), while high (low) FeO contents are associated with high (low) Al_2O_3 contents and oxidation states.
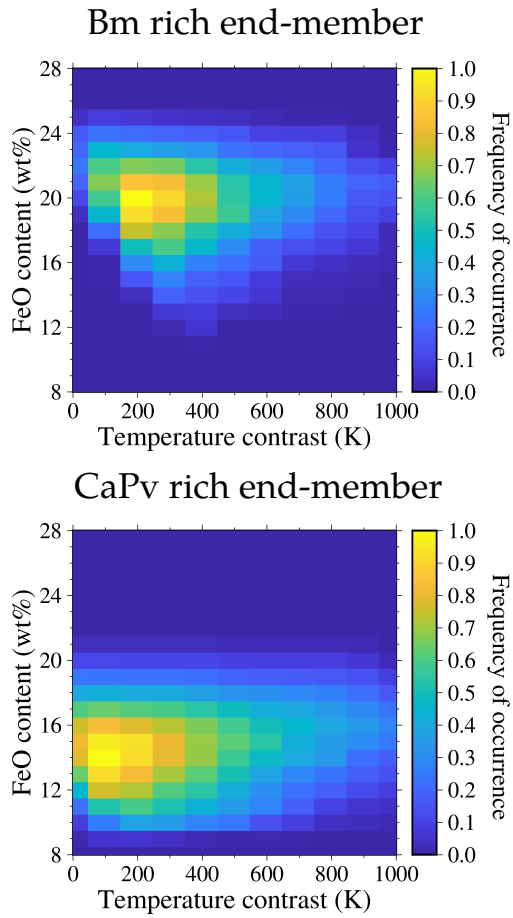
Figure 4: 2D histograms showing the distribution of the models corresponding to the Bm-rich case (top panels) and CaPv-rich case (bottom panels) as a function of the temperature contrast and FeO content.

Acknowledgments

Reference

References

Andrault, D., Bolfan-Casanova, N., Lo Nigro, G., Bouhifd, M.A., Garbarino, G., Mezouar, M., 2011. Solidus and liquidus profiles of chondritic mantle: Implication for melting of the Earth across its history. Earth and Planetary Science Letters 304, 251–259. doi:`10.1016/j.epsl.2011.02.006`.

Andrault, D., Petitgirard, S., Lo Nigro, G., Devidal, J.L., Veronesi, G., Garbarino, G., Mezouar, M., 2012. Solid–liquid iron partitioning in Earth's deep mantle. Nature 487, 354–357. doi:`10.1038/nature11294`.

Arndt, N., Lesher, M.C., Barnes, S.J., 2008. Komatiite. Cambridge University Press.

Ballmer, M.D., Lourenço, D.L., Hirose, K., Caracas, R., Nomura, R., 2017. Reconciling magma-ocean crystallization models with the present-day structure of the Earth's mantle. Geochemistry, Geophysics, Geosystems 18, 2785–2806. doi:`10.1002/2017GC006917`.

Ballmer, M.D., Schumacher, L., Lekic, V., Thomas, C., Ito, G., 2016. Compositional layering within the large low shear-wavevelocity provinces in the lower mantle. Geochemistry, Geophysics, Geosystems 17, 5056–5077. doi:`10.1002/2016GC006605`.

Bina, C.R., Helffrich, G.R., 1992. Calculation of Elastic Properties from Thermodynamic Equation of State Principles. Annual Review of Earth and Planetary Sciences 20, 527–552. doi:`10.1146/annurev.ea.20.050192.002523`.

Boujibar, A., Bolfan-Casanova, N., Andrault, D., Bouhifd, M.A., Trcera, N., 2016. Incorporation of Fe^{2+} and Fe^{3+} in bridgmanite during magma ocean crystallization. American Mineralogist 107, 1560–1570. doi:`10.2138/am-2016-5561`.

Boukaré, C.E., Parmentier, E.M., Parman, S.W., 2018. Timing of mantle overturn during magma ocean solidification. Earth and Planetary Science Letters 491, 216–225. doi:`10.1016/j.epsl.2018.03.037`.

Boukaré, C.E., Ricard, Y., 2017. Modeling phase separation and phase change for magma ocean solidification dynamics. Geochemistry, Geophysics, Geosystems 18, 3385–3404. doi:`10.1002/2017GC006902`.

Boukaré, C.E., Ricard, Y., Fiquet, G., 2015. Thermodynamics of the MgO-FeO-SiO_2 system up to 140 GPa: Application to the crystallization of Earth's magma ocean. Journal of Geophysical Research: Solid Earth 120, 6085–6101. doi:`10.1002/2015JB011929`.

Caracas, R., Hirose, K., Nomura, R., Ballmer, M.D., 2019. Melt–crystal density crossover in a deep magma ocean. Earth and Planetary Science Letters 516, 202–211. doi:`10.1016/j.epsl.2019.03.031`.

Catalli, K., Shim, S.H., Dera, P., Prakapenka, V.B., Zhao, J., Sturhahn, W., Chow, P., Xiao, Y., Cynn, H., Evans, W.J., 2011. Effects of the Fe^{3+} spin transition on the properties of aluminous perovskite — new insights for lower-mantle seismic heterogeneities. Earth and Planetary Science Letters 310, 293–302. doi:`10.1016/j.epsl.2011.08.018`.

Catalli, K., Shim, S.H., Prakapenka, V.B., 2009. Thickness and Clapeyron slope of the post-perovskite boundary. Nature 462, 782–786. doi:`10.1038/nature08598`.

Catalli, K., Shim, S.H., Prakapenka, V.B., Zhao, J., Sturhahn, W., Chow, P., Xiao, Y., Liu, H., Cynn, H., Evans, W.J., 2010. Spin state of ferric iron in $MgSiO_3$ perovskite

and its effect on elastic properties. Earth and Planetary Science Letters 289, 68–75. doi:`10.1016/j.epsl.2009.10.029`.

Cobden, L., Thomas, C., Trampert, J., 2015. Seismic Detection of Post-perovskite Inside the Earth. Springer International Publishing. pp. 391–440. doi:`10.1007/978-3-319-15627-9_13`.

Davies, D.R., Goes, S., Davies, J.H., Schuberth, B.S.A., Bunge, H.P., Ristema, J., 2012. Reconciling dynamic and seismic models of Earth's lower mantle: The dominant role of thermal heterogeneity. Earth and Planetary Science Letters 353–354, 253–269. doi:`10.1016/j.epsl.2012.08.016`.

Deschamps, F., Cobden, L., Tackley, P.J., 2012. The primitive nature of large low shear-wave velocity provinces. Earth and Planetary Science Letters 349–350, 198–208. doi:`10.1016/j.epsl.2012.07.012`.

Deschamps, F., Konishi, K., Fuji, N., Cobden, L., 2019. Radial thermo-chemical structure beneath Western and Northern Pacific from seismic waveform inversion. Earth and Planetary Science Letters 520, 153–163. doi:`10.1016/j.epsl.2019.05.040`.

Deschamps, F., Tackley, P.J., 2008. Searching for models of thermo-chemical convection that explain probabilistic tomography I. Principles and influence of rheological parameters. Physics of the Earth and Planetary Interiors 171, 357–373. doi:`10.1016/j.pepi.2008.04.016`.

Elkins-Tanton, L.T., Parmentier, E.M., Hess, P.C., 2003. Magma ocean fractional crystallization and cumulate overturn in terrestrial planets: Implications for Mars. Meteoritics & Planetary Science 38, 1753–1771. doi:`10.1111/j.1945-5100.2003.tb00013.x`.

Fei, Y.W., Zhang, L., Corgne, A., Watson, H.C., Ricolleau, A., Meng, Y., Prakapenka,

V.B., 2007. Spin transition and equations of state of (Mg, Fe)O solid solutions. Geophysical Research Letters 34, L17307. doi:10.1029/2007GL030712.

Gale, A., Dalton, C.A., Langmuir, C.H., Su, Y., Schilling, J.G., 2013. The mean composition of ocean ridge basalts. Geochemistry, Geophysics, Geosystems 14, 489–518. doi:10.1029/2012GC004334.

Garnero, E.J., McNamara, A.K., Shim, S.H., 2016. Continent-sized anomalous zones with low seismic velocity at the base of Earth's mantle. Nature Geoscience 9, 484–489. doi:10.1038/ngeo2733.

Hirose, K., Morard, G., Sinmyo, R., Umemoto, K., Hernlund, J., Helffrich, G., Labrosse, L., 2017. Crystallization of silicon dioxide and compositional evolution of the Earth's core. Nature 543, 99–102. doi:10.1038/nature21367.

Houser, C., Masters, G., Shearer, P., Laske, G., 2008. Shear and compressional velocity models of the mantle from cluster analysis of long-period waveforms. Geophysical Journal International 174, 195–212. doi:10.1111/j.1365-246X.2008.03763.x.

Ishii, M., Tromp, J., 1999. Normal-mode and free-air gravity constraints on lateral variations in velocity and density of Earth's mantle. Science 285, 1231–1236. doi:10.1126/science.285.5431.1231.

Jackson, I., Rigden, S.M., 1996. Analysis of P-V-T data: constraints on the thermoelastic properties of high-pressure minerals. Physics of the Earth and Planetary Interiors 96, 85–112. doi:10.1016/0031-9201(96)03143-3.

Koelemeijer, P., Ritsema, J., Deuss, A., van Heijst, H.J., 2016. SP12RTS: a degree-12 model of shear- and compressional-wave velocity for Earth's mantle. Geophysical Journal International 204, 1024–1039. doi:10.1093/gji/ggv481.

Labrosse, S., Hernlund, J.W., Coltice, N., 2007. A crystallizing dense magma ocean at the base of the Earth's mantle. Nature 450, 866–869. doi:10.1038/nature06355.

Lau, H.C.P., Mitrovica, J.X., Davis, J.L., Tromp, J., Yang, H.Y., Al-Attar, D., 2017. Tidal tomography constrains Earth's deep-mantle buoyancy. Nature 551, 321–326. doi:`10.1038/nature24452`.

Li, L., Weidner, D.J., Brodholt, J.P., Alfè, D., Price, G.D., Caracas, R., Wentzcovitch, R., 2006. Elasticity of CaSiO$_3$ perovskite at high pressure and high temperature. Physics of the Earth and Planetary Interiors 155, 249–259. doi:`10.1016/j.pepi.2005.12.006`.

Li, Y., Deschamps, F., Tackley, P.J., 2014. The stability and structure of primordial reservoirs in the lower mantle: insights from models of thermochemical convection in three-dimensional spherical geometry. Geophysical Journal International 199, 914–930. doi:`10.1093/gji/ggu295`.

Masters, G., Laske, G., Bolton, H., Dziewonski, A., 2000. The relative behavior of shear velocity, bulk sound speed, and compressional velocity in the mantle: implications for chemical and thermal structure. AGU. volume 117 of *Geophysical Monograph Series*. pp. 63–87. doi:`10.1029/GM117p0063`.

McDonough, W.F., Sun, S.S., 1995. The composition of the Earth. Chemical Geology 120, 223–253. doi:`10.1016/0009-2541(94)00140-4`.

McKay, D.S., Heiken, G., Basu, A., Blanford, G., Simon, S., Reedy, R., French, B.M., Papike, J., 1991. The lunar regolith. Cambridge Univ. Press. pp. 285–356.

McNamara, A.K., Zhong, S., 2005. Thermochemical structures beneath Africa and the Pacific Ocean. Nature 437, 1136–1139. doi:`10.1038/nature04066`.

Murakami, M., Ohishi, Y., Hirao, N., Hirose, K., 2009. Elasticity of MgO to 130 GPa: Implications for lower mantle mineralogy. Earth and Planetary Science Letters 277, 123–129. doi:`10.1016/j.epsl.2008.10.010`.

Murakami, M., Ohishi, Y., Hirao, N., Hirose, K., 2012. A perovskitic lower mantle inferred from high-pressure, high-temperature sound velocity data. Nature 485, 90–94. doi:`10.1038/nature11004`.

Nakagawa, T., Tackley, P.J., Deschamps, F., Connolly, J.A.D., 2010. The influence of MORB and harzburgite composition on thermo-chemical mantle convection in a 3-D spherical shell with self-consistently calculated mineral physics. Earth and Planetary Science Letters 296, 403–412. doi:`10.1016/j.epsl.2010.05.026`.

Nomura, R., Ozawa, H., Tateno, S., Hirose, K., Hernlund, J., Muto, S., Ishii, H., Hiraoka, N., 2011. Spin crossover and iron-rich silicate melt in the Earth's deep mantle. Nature 473, 199–202. doi:`10.1038/nature09940`.

Piet, H., Badro, J., Nabiei, F., Dennenwaldt, T., Shim, S.H., Cantoni, M., Hébert, C., Gillet, P., 2016. Spin and valence dependence of iron partitioning in Earth's deep mantle. Proceedings of the National Academy of Sciences of the United States of America 113, 11127–11130. doi:`10.1073/pnas.1605290113`.

Ricolleau, A., Perillat, J.P., Fiquet, G., Daniel, I., Matas, J., Addad, A., Menguy, N., Cardon, H., Mezouar, M., Guignot, N., 2010. Phase relations and equation of state of a natural MORB: Implications for the density profile of subducted oceanic crust in the Earth's lower mantle. Journal of Geophysical Research 115, B08202. doi:`10.1029/2009JB006709`.

Samuel, H., Farnetani, C.G., Andrault, D., 2005. Heterogeneous lowermost mantle: compositional constraints and seismological observables. American Geophysical Union (AGU). pp. 101–116. doi:`10.1029/160GM08`.

Shim, S.H., 2008. The Postperovskite Transition. Annual Review of Earth and Planetary Sciences 36, 569–599. doi:`10.1146/annurev.earth.36.031207.124309`.

Shukla, G., Cococcioni, M., Wentzcovitch, R.M., 2016. Thermoelasticity of Fe^{3+}-

and Al-bearing bridgmanite: Effects of iron spin crossover. Geophysical Research Letters 43, 5661–5670. doi:`10.1002/2016GL069332`.

Shukla, G., Wu, Z., Hsu, H., Floris, A., Cococcioni, M., Wentzcovitch, R.M., 2015. Thermoelasticity of Fe^{2+}-bearing bridgmanite. Geophysical Research Letters 42, 1741–1749. doi:`10.1002/2014GL062888`.

Solomatov, V., 2015. Magma Oceans and Primordial Mantle Differentiation. Elsevier. volume 9 of *Treatise on Geophysics*. pp. 81–104. doi:`10.1016/B978-0-444-53802-4.00155-X`.

Su, W.J., Woodward, R.L., Dziewonski, A.M., 1994. Degree 12 model of shear velocity heterogeneity in the mantle. Journal of Geophysical Research 99, 6945–6980. doi:`10.1029/93JB03408`.

Sun, N., Wei, W., Han, S., Song, J., Li, X., Duan, Y., Prakapenka, V.B., Mao, Z., 2018. Phase transition and thermal equations of state of (Fe, Al)-bridgmanite and post-perovskite: Implication for the chemical heterogeneity at the lowermost mantle. Earth and Planetary Science Letters 490, 161–169. doi:`10.1016/j.epsl.2018.03.004`.

Tackley, P.J., 1998. Three-dimensional simulations of mantle convection with a thermochemical CMB boundary layer: D"?, in: Gurnis, M., Wysession, M.E., Knittle, E., Buffett, B.A. (Eds.), The Core-Mantle Boundary Region. AGU, pp. 231–253.

Tackley, P.J., 2012. Dynamics and evolution of the deep mantle resulting from thermal, chemical, phase and melting effects. Earth-Science Reviews 110, 1–25. doi:`10.1016/j.earscirev.2011.10.001`.

Tateno, S., Hirose, K. Ohishi, Y., 2014. Melting experiments on peridotite to lowermost mantle conditions. Journal of Geophysical Research: Solid Earth 119, 4684–4694. doi:`10.1002/2013JB010616`.

Thomson, A.R., Crichton, W.A., Brodholt, J.P., Wood, I.G., Siersch, N.C., Muir, J.M.R., Dobson, D.P., Hunt, S.A., 2019. Seismic velocities of CaSiO$_3$ perovskite can explain LLSVPs in Earth's lower mantle. Nature 572, 643–647. doi:`10.1038/s41586-019-1483-x`.

Tolstikhin, I.N., Hofmann, A.W., 2005. Early crust on top of the Earth's core. Physics of the Earth and Planetary Interiors 148, 109–130. doi:`10.1016/j.pepi.2004.05.011`.

Trampert, J., Deschamps, F., Resovsky, J., Yuen, D., 2004. Probabilistic Tomography Maps Chemical Heterogeneities Throughout the Lower Mantle. Science 306, 853–856. doi:`10.1126/science.1101996`.

Tronnes, R.G., Frost, D.J., 2002. Peridotite melting and mineral–melt partitioning of major and minor elements at 22–24.5 GPa. Earth and Planetary Science Letters 197, 117–131. doi:`10.1016/S0012-821X(02)00466-1`.

Vilella, K., 2020. Constraints on the composition and temperature of LLSVPs from seismic properties of lower mantle minerals. Mendeley Data , Version 1doi:`10.17632/9w3n24sz6c.1`.

Vilella, K., Shim, S.H., Farnetani, C.G., Badro, J., 2015. Spin state transition and partitioning of iron: effects on mantle dynamics. Earth and Planetary Science Letters 417, 57–66. doi:`10.1016/j.epsl.2015.02.009`.

Walter, M.J., Nakamura, E., Tronnes, R.G., Frost, D.J., 2004. Experimental constraints on crystallization differentiation in a deep magma ocean. Geochimica et Cosmochimica Acta 68, 4267–4284. doi:`10.1016/j.gca.2004.03.014`.

Wang, W., Xu, Y., Sun, D., Ni, S., Wentzcovitch, R., Wu, Z., 2020. Velocity and density characteristics of subducted oceanic crust and the origin of lower-mantle heterogeneities. Nature Communications 11, 64. doi:`10.1038/s41467-019-13720-2`.

Wu, Z., Justo, J.F., Wentzcovitch, R.M., 2013. Elastic Anomalies in a Spin-Crossover System: Ferropericlase at Lower Mantle Conditions. Physical Review Letters 110, 228501. doi:`10.1103/PhysRevLett.110.228501`.